

ConvRML: High-Quality Lensless Imaging with Random Multi-Focal Lenslets

Leyla A. Kabuli[†], Clara S. Hung[†], Vasilisa Ponomarenko,
Eric Markley, Laura Waller

Department of Electrical Engineering and Computer Sciences,
University of California, Berkeley, California 94720, USA.

^{*}Corresponding author(s). E-mail(s): lakabuli@berkeley.edu;

[†]These authors contributed equally to this work.

Abstract

Mask-based lensless imagers use simple optics and computational reconstruction to design compact form factor cameras with compressive imaging ability. However, these imagers generally suffer from poor reconstruction quality. Here, we describe several advances in both hardware and software that result in improved lensless imaging quality. First, we use a precision-manufactured random multi-focal lenslet (RML) phase mask to produce improved measurements with reduced multiplexing. Next, we implement a ConvNeXt-based reconstruction architecture, which provides up to 6.68 dB improvement in peak signal-to-noise ratio over state-of-the-art attention-based architectures. Finally, we establish a parallel imaging setup that simultaneously images a scene with RML, diffuser and lens systems, with which we collect datasets with 100,000 measurements for each system, to be used for reconstruction model training and evaluation. Using this standardized system, we quantify the improved measurement quality of the RML compared to a diffuser using the modulation transfer function and mutual information. Our ConvRML system benefits from both the optical and the computational developments presented in this work, and our contributions establish resources to support continued development of high-quality, compact, and compressive lensless imagers.

1 Introduction

Computational imaging systems jointly design optical hardware and computational algorithms to push the limits of image capture and interpretation. In mask-based lensless imaging, a traditional lens is replaced by a thin amplitude or phase mask that patterns incoming light into a multiplexed sensor measurement, which is then computationally decoded to reconstruct an image. This two-part design offers a flexible alternative to conventional optics, enabling compact, low-cost, and single-shot systems that support compressive encoding and recovery, including three-dimensional (3D) [1–4] and extended field-of-view (FOV) [5–8] imaging. With these capabilities, lensless imaging systems are promising for applications ranging from photography [1, 2] and machine vision [9] to *in vivo* microscopy [10, 11] and mesoscopy [3, 12].

A central challenge in lensless imaging is image quality. Ill-posed inverse problems, model mismatch, and compressive encoding all result in lower reconstruction quality than traditional lens systems. Although reconstruction algorithms with increased computational power can partially compensate, their performance is fundamentally limited by the amount of information encoded in the measurements [6]. Improving lensless image quality therefore requires developing both optical encoders that produce better measurements *and* algorithms that can utilize those measurements.

A primary research direction in lensless imaging has focused on optical encoder design to improve measurement quality. Phase masks have gained widespread use due to their light efficiency compared to amplitude masks [13]. Initial phase mask-based systems used off-the-shelf diffusers [1] or heuristically-designed masks [2] that produce large distributed point spread functions (PSFs). We refer to PSFs that distribute light over a large area as *high multiplexing*, since they map each point in the scene to many pixels on the sensor, resulting in a high-multiplexing measurement. Multiplexing is necessary for compressed sensing and often useful because of its redundancy, but for dense natural scenes, high multiplexing levels reduce measurement contrast, limiting the image quality of the system. As a result, optical designs have shifted toward using less multiplexing; for example, regular microlens arrays [3, 5, 14] and random lenslet arrays [4, 6, 10, 11, 15] produce PSFs that span a large area but have only a few sparse points. Implementable designs have been constrained by fabrication limitations, with previous systems relying on hand-assembled [11] or manually-fabricated optical elements [10, 15, 16], which limit precision in surface control and reproducibility. As precision fabrication of freeform optical elements becomes increasingly accessible, lenslet-based designs offer a clear path to improved lensless measurement quality.

A complementary direction has focused on developing reconstruction algorithms to better utilize multiplexed measurements. Decoders have shifted from iterative algorithms with physics-based constraints [17, 18] to hybrid [19–21] or pure deep learning-based approaches [22, 23] with increasing computational and architectural complexity, including attention-based architectures designed to explicitly capture long-range dependencies [23]. Much of this algorithmic development has progressed independently of optical design, with new architectures typically evaluated on existing open-source datasets [9, 19, 23, 24]. However, these datasets consist of measurements taken with high-multiplexing PSFs, rather than newer, lower-multiplexing lenslet

designs. As a result, it remains unknown which architectures can best utilize higher-quality measurements, and how much reconstructions can improve when algorithms are paired with better optical encoders.

In this work, we present ConvRML, a lensless imaging system that pairs precision-manufactured optical elements with modern convolutional neural networks and standardized training datasets to advance high-quality lensless imaging (Fig. 1). We show that a random multi-focal lenslet (RML) phase mask improves measurement quality, and can be precisely fabricated using recent advances in optical manufacturing. Our deep learning-based reconstruction uses a ConvNeXt architecture, which achieves up to 6.68 dB peak signal-to-noise ratio (PSNR) improvement over state-of-the-art attention-based architectures, successfully handling long-range dependencies in multiplexed measurements even with limited training data.

To facilitate comprehensive evaluation and continued system development, we contribute multiple datasets each with 100,000 measurements, captured using a standardized parallel hardware setup that enables controlled comparison across optical encoders and reconstruction algorithms. Using this setup, we quantify the performance improvements of ConvRML relative to a diffuser phase mask in both optical encoding and image reconstruction, and present high-quality reconstructions for both systems that generalize to real-world objects. Together, our work demonstrates that improved measurement quality paired with powerful algorithms facilitates maximum reconstruction performance for lensless imaging systems, and establishes resources for continued lensless imaging system development.

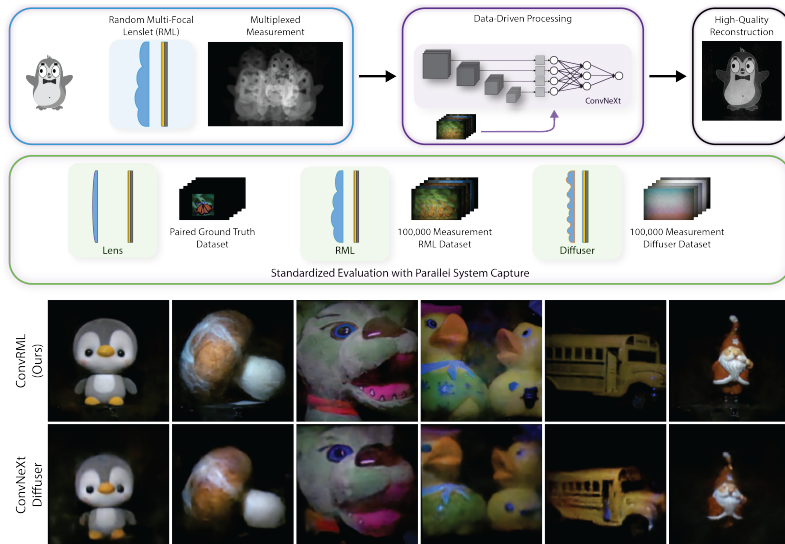


Fig. 1 ConvRML system overview. (top) Our high-quality lensless imaging system combines a random multi-focal lenslet (RML) phase mask with a ConvNeXt reconstruction architecture. (middle) To facilitate data-driven training of reconstruction architectures and controlled system comparisons between a lens, a diffuser, and our RML, we collect and open-source datasets with 100,000 measurements for each system. (bottom) ConvNeXt models trained on displayed image datasets for the RML and diffuser lensless imagers produce high-quality reconstructions of real-world objects.

2 Results

Lenses collect and focus light such that a point in the scene is imaged to a focused point on the sensor. For a fixed numerical aperture (NA), reducing the focal length of the lens produces a more compact system but proportionally reduces the FOV (Fig. 2a). Achieving both a compact system and a wide FOV requires high-NA optics, which are typically thick, expensive and prone to aberrations. In contrast, lensless imagers exchange the lens for a thin multiplexing element placed close to the sensor, maintaining both a compact form factor and a wide FOV (Fig. 2a). As a consequence, points in the scene must be imaged onto multiple pixels of the sensor; this multiplexing effect is why lensless imagers require a decoding algorithm for image reconstruction.

Each imaging system can be characterized by its point spread function (PSF). With no multiplexing, a conventional lens system produces a point PSF, whose width is determined by the NA of the system. Gaussian diffusers [1] instead refract light using bumpy surfaces, producing a high-multiplexing caustic pattern (Fig. 2b). Lenslet-based masks use arrays of lenslets that produce a lower-multiplexing, high-contrast PSF consisting of multiple focal spots with minimal diffuse background.

Measurements are generated following the image formation model

$$\mathbf{y} = \mathcal{N}(\text{crop}(\mathbf{x} * \mathbf{h})), \quad (1)$$

where the object \mathbf{x} is convolved with the system PSF \mathbf{h} , cropped by the sensor extent, and corrupted by detection noise $\mathcal{N}(\cdot)$, which can be modeled as signal-independent read noise or signal-dependent shot noise [25, 26]. At shorter working distances or with a larger FOV, off-axis incident light can result in spatially-varying PSFs [27] that require a more complicated forward model [10, 28]. Here, we work with photography-scale lensless imaging at cm-scale working distances, where the convolution model is a sufficient approximation [1]. However, our deep learning-based reconstruction methods do not explicitly assume spatial invariance or a specific forward model, so they may be flexible enough to implicitly learn spatially-varying PSFs.

2.1 Random multi-focal lenslet phase mask

Our lensless imaging system uses a random multi-focal lenslet (RML) phase mask as the optical encoder, which consists of overlapping lenslets with a range of focal lengths placed at pseudo-random positions across the aperture. Compared to a regular lenslet array, pseudo-random lenslet positions minimize correlations between shifted copies of the system PSF, which reduces ambiguity during reconstruction [10, 16, 29]. Limiting the number of lenslets reduces multiplexing to improve measurement quality for dense natural scenes, and high fill factor across the mask aperture minimizes stray light leakage. With recent advances in high-resolution, large-area two-photon lithography [30], these designs can now be precisely, quickly, and reproducibly fabricated.

Because our phase mask has lenslets focused at various depths, the imager maintains sharp PSF features even with variations in the sensor-to-mask distance.

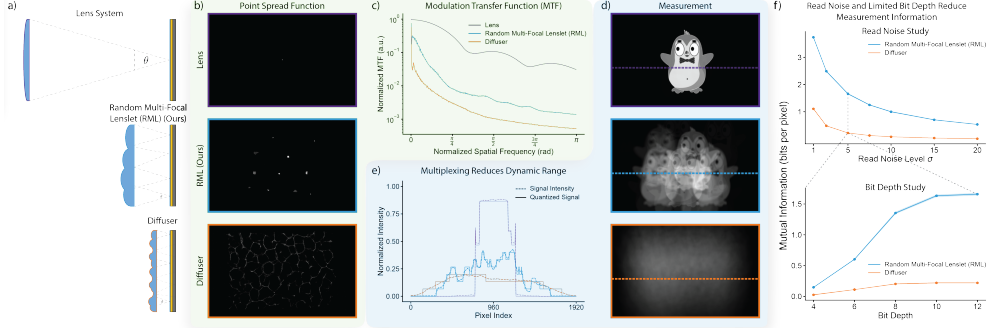


Fig. 2 Random multi-focal lenslet (RML) phase masks result in good measurement quality. a) Illustration and b) experimentally-measured point spread functions (PSFs) for different optical encoders with a fixed numerical aperture θ . A lens focuses light to a single focal point, with the field of view (FOV) decreasing for shorter focal lengths. The RML distributes light across a small number of focal points, preserving a wide FOV with minimal diverging light. The diffuser both focuses and scatters light, resulting in a high-multiplexing caustic pattern. PSFs are contrast stretched for visualization. c) Modulation transfer functions (MTFs) for each design, with the lens system serving as an ideal reference. The RML has improved frequency transfer compared to the diffuser, especially at high spatial frequencies. d) Simulated measurements for each imaging system. The high-multiplexing diffuser PSF generally results in lower contrast measurements, while RML measurements preserve larger local intensity variations. e) Cross-sections of each measurement along with dashed lines showing the loss of dynamic range with quantization. f) Mutual information evaluation of the effects of read noise and limited bit depth. The RML maintains higher information than the diffuser as noise increases (top) and retains nonzero information at low bit depths while the diffuser has approximately zero information (bottom).

Compared to caustic masks or uni-focal lenslet arrays, which should be precisely positioned at a specific distance for sharp PSF features; this reduces our design's sensitivity to system alignment [31].

Direct comparison to previously-proposed lensless imagers is challenging because of variations in system implementation. Differences in sensor specifications, system magnification, compactness, and illumination conditions all affect measurement quality, confounding optical encoder comparisons. To isolate the effect of the optical encoder, we establish a parallel imaging setup in which designs are evaluated under identical imaging conditions with the same sensor, illumination, magnification, and careful alignment (Fig. 3a). In our standardized evaluation, we compare our RML to a diffuser and a lens, which serves as a reference for target image quality without multiplexing.

Using the experimentally captured PSFs shown in Fig. 2b, we calculate the modulation transfer function (MTF) for each system to evaluate the frequency transfer characteristics of the optical encoder (Fig. 2c). As expected, both lensless imaging systems have worse frequency transfer than the lens due to their multiplexed PSFs. The RML has higher frequency transfer than the diffuser across all spatial frequencies due to the reduced multiplexing and sharp focal spots in its PSF. The RML similarly outperforms PhlatCam (Supplement Fig. S3), although we note that the PhlatCam PSF is from the original system [2], captured under different experimental imaging conditions.

High-multiplexing encoders generally reduce the contrast in measurements, requiring costly sensors with high bit depth [32] to compensate for increased sensitivity to sensor noise and quantization error. Comparing simulated measurements for each system (Fig. 2d), the RML generates shifted object copies that preserve fine details while the diffuser produces a measurement that has no visually interpretable object structure. To illustrate, we plot measurement cross-sections in Fig. 2e. The diffuser has minimal signal variation, whereas the RML produces high-contrast signals and the lens has sharp transitions corresponding to object edges. To illustrate the effects of limited sensor bit depth, we overlay a 4-bit quantization of the signals (dashed lines, Fig. 2e). With heavy quantization, most signal variations for the diffuser fall within a single quantization bin and are effectively lost, whereas the RML maintains both distinguishable features and multiplexing ability.

Finally, we evaluate measurement quality using mutual information (MI), which quantifies how much object information is available in measurements, capturing the combined effects of optical encoding, object statistics, and measurement noise [6, 33]. We first study the effect of read noise by calculating MI for simulated measurements of natural images [34] with increasing standard deviations σ of read noise (Fig. 2f, top). Across all noise levels, the RML encodes more information than the diffuser. Then, we evaluate the effect of quantization noise resulting from limited bit depth. For a fixed read noise level ($\sigma = 5$ photons), we quantize measurements to effective bit depths of 4 to 12 bits and calculate MI in each case (Fig. 2f, bottom), finding that the RML continues to outperform the diffuser across all bit depths. At 4 bits, the diffuser retains almost no information, while the RML measurements continue to encode object information,. This result is consistent with the dynamic range visualization in Fig. 2e, where most diffuser signal variations are lost to quantization.

2.2 100,000 measurement Parallel Lensless Dataset

Modern data-driven reconstruction architectures, such as attention-based architectures or large convolutional neural networks, require large training datasets. For example, recent transformer-based models were trained with 60,000 lensless measurements [23]. However, available experimental datasets for phase mask-based systems have only 10,000 measurements for PhlatCam [24] and 25,000 measurements for DiffuserCam [19], and no open-source datasets are available for lenslet-based systems.

Here, we introduce an open-source experimental dataset of 100,000 measurements for multiple imaging systems: our RML lensless imager, a diffuser lensless imager, and a conventional lens system (which we treat as ground truth). To automate parallel data acquisition, we use synchronized hardware and software control (Fig. 3a). Each imaging system uses the same sensor, illumination, and object magnification to ensure that differences in system performance are due to the optical encoder rather than experimental variations. Together, our Parallel Lensless Dataset (PLD) provides the largest open-source experimental lensless imaging datasets to date. We use these datasets to provide a standardized system-level comparison between imagers, and hope that they serve as resources to facilitate future development of reconstruction architectures.

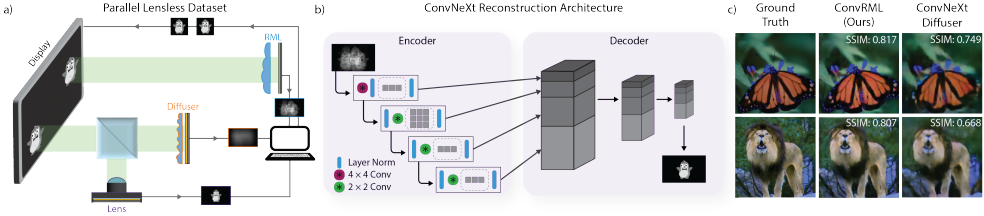


Fig. 3 Standardized experimental comparison of RML and diffuser systems. a) Parallel dataset acquisition with RML, diffuser, and lens (ground truth) systems under identical imaging conditions facilitates standardized comparisons. b) The ConvNeXt-based reconstruction architecture creates multi-scale feature maps, which are concatenated and progressively compressed. c) Example reconstructions comparing ground truth, our RML with ConvNeXt reconstruction (ConvRML), and a diffuser with ConvNeXt reconstruction. Using an RML achieves higher reconstruction quality than the diffuser, as quantified by the structural similarity index measure (SSIM).

2.3 ConvRML system evaluation

We now evaluate our complete ConvRML imaging system, incorporating improved optical measurements from the RML, a modern ConvNeXt architecture for reconstruction [35], and our open-source dataset.

Lensless image reconstruction is challenging in part due to the spatial extent of system PSFs, which produce multiplexed measurements with long-range dependencies. ConvNeXt is a convolutional neural network architecture that achieves large effective receptive fields through cascaded convolutional layers while maintaining moderate computational requirements [35, 36]. We expect this neural network, with large receptive fields capable of processing long-range dependencies from multiplexing PSFs, to be suitable for lensless image reconstruction. Our reconstruction architecture combines the ConvNeXt encoder, which consists of a series of downsampling blocks, with concatenation and compression operations in the decoder (Fig. 3b).

We train separate ConvNeXt models for the RML and diffuser lensless imagers, using 50,000 measurements from the PLD for each system. By keeping all training procedures and dataset sizes consistent, we isolate the interaction between optical encoding and reconstruction architecture.

Figure 3c shows reconstruction results using our ConvNeXt reconstruction models with both RML and diffuser systems. ConvRML reconstructions better recover fine spatial detail, contrast, and color fidelity, with test set improvements of 2.99 dB PSNR and 0.116 structural similarity index measure (SSIM) relative to the diffuser system. Since this comparison controls for algorithmic variability, dataset size, and experimental conditions, we can conclude that the RML measurements directly translate to higher-quality reconstructions than with the diffuser system.

2.4 Comparison of reconstruction architectures

Next, we isolate the effects of reconstruction architecture and training data. We compare multiple modern deep learning architectures, including attention-based architectures, on both an existing benchmark dataset as well as our contributed datasets, in

order to determine how dataset size and multiplexing levels influence the performance of different architectures.

For comparison to our ConvNeXt architecture, we provide lensless imaging implementations of several attention-based architectures. First, we contribute a lightweight Vision Transformer (ViT) [37]. This small attention-based architecture transforms the input into a series of flattened image patches, which are processed with global self-attention layers to capture long-range dependencies. Second, we contribute a Swin Transformer [38], a large-capacity architecture that utilizes shifted-window attention for a hierarchical representation that captures both local and global features. We also compare to the Lensless Imaging Transformer [23], which is a moderate-capacity attention-based reconstruction architecture designed for lensless imaging. As a baseline for deep learning reconstruction, we include the standard U-Net architecture used in lensless imaging [19].

We first compare reconstruction architectures by training all models on the DiffuserCam Lensless Mirflickr Dataset (DLMD) [19], which consists of 25,000 measurements from a high-multiplexing diffuser. This widely-used benchmark for data-driven lensless imaging reconstruction provides a standardized reference for direct model comparison.

We evaluate our ConvNeXt, the Lensless Imaging Transformer [23], the Swin Transformer, and the Vision Transformer against the U-Net baseline reported for the DLMD [19]. Reconstruction results are shown in Fig. 4. Compared to the ground truth images (bottom row), ConvNeXt has the highest reconstruction quality, with improved color fidelity and recovery of fine image details. The compact Vision Transformer and the large Swin Transformer both exhibit visible blocking artifacts and blurred image features that are qualitatively worse than the U-Net. The Lensless Imaging Transformer provides improved results over the U-Net, especially in color fidelity, but has worse resolution than ConvNeXt.

Quantitative performance metrics are reported in Table 1. ConvNeXt achieves the highest PSNR and SSIM among all evaluated models while maintaining moderate model capacity, with more parameters than the Lensless Imaging Transformer, but fewer parameters than the Swin Transformer. These results demonstrate that a carefully-designed convolutional architecture can outperform attention-based architectures on a high-multiplexing system with a moderately-sized dataset.

Table 1 Reconstruction quality and parameter count for models evaluated on the DiffuserCam Lensless Mirflickr Dataset [19].

Model	PSNR \uparrow	SSIM \uparrow	Parameter count
U-Net [19]	17.29	0.583	10.6M
Vision Transformer	21.26	0.630	1.0M
Swin Transformer	21.19	0.633	59.4M
Lensless Imaging Transformer [23]	22.32	0.671	16.1M
ConvNeXt (Ours)	25.37	0.762	36M

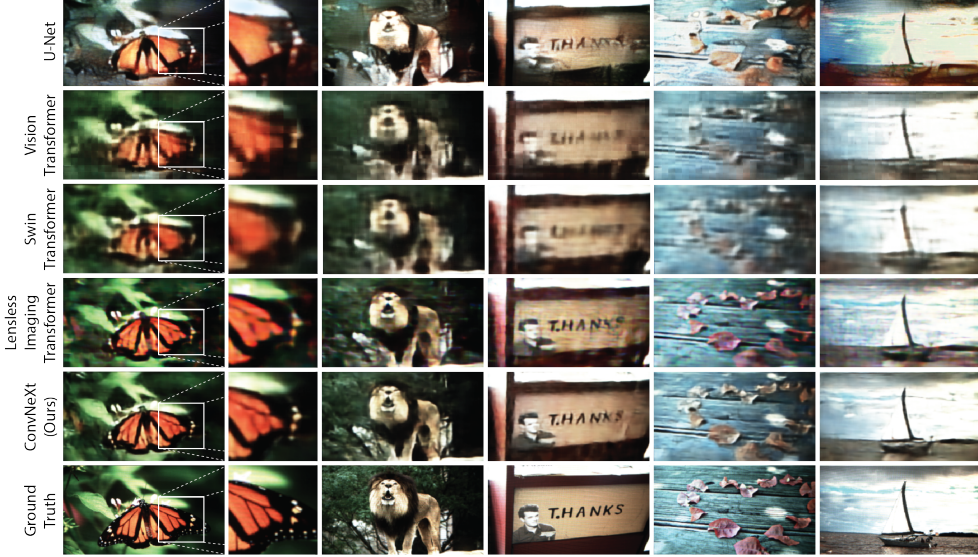


Fig. 4 Comparison of reconstruction models evaluated on the DiffuserCam Lensless Mirflickr Dataset [19]. Our ConvNeXt model provides reconstructions that most closely match ground truth images for this high-multiplexing diffuser system.

Next, we compare reconstruction architectures for our lower-multiplexing RML using a larger measurement dataset. Although ConvNeXt outperformed attention-based models on the DLMD benchmark, it is possible that the 25,000 measurement DLMD dataset may have been insufficient for training the attention-based architectures. Therefore, we investigate whether increasing dataset size changes the relative performance of these models for RML measurements.

We study tradeoffs between model capacity, dataset size, and training cost by training the ConvNeXt model on subsets ranging from 25,000 to 100,000 RML measurements from the PLD (Supplement Fig. S1). Reconstruction quality improves up to 50,000 measurements and then plateaus, while training time increases substantially, indicating that the capacity of our model is best matched to a dataset size of 50,000 measurements, which we adopt for all subsequent evaluations.

Using this dataset size, we compare ConvNeXt to the Swin Transformer, the Lensless Imaging Transformer, and the Vision Transformer for RML measurement reconstruction, as well as ConvNext diffuser measurement reconstructions as a baseline. Reconstruction examples are shown in Fig. 5 and quantitative performance metrics are reported in Table 2, with ConvNeXt consistently achieving the highest reconstruction quality. All models benefit from the larger training dataset, although the compact Vision Transformer still suffers from patching artifacts as previously seen in Fig. 4. Among attention-based models, the Lensless Imaging Transformer best recovers fine details and structure, although poor color fidelity results in reduced metric values, especially PSNR. The reconstruction quality of attention-based models for

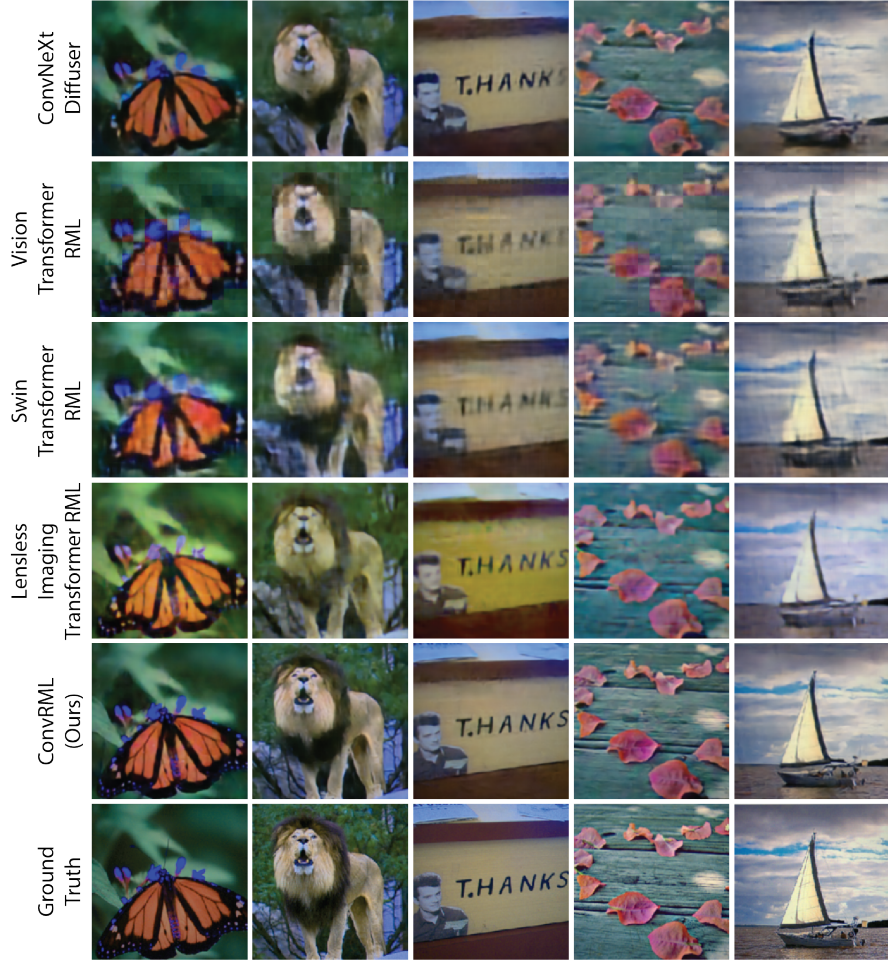


Fig. 5 Comparison of reconstruction models evaluated on our Parallel Lensless Dataset. Our ConvRML system provides reconstructions that are best matched to ground truth images for the low-multiplexing RML dataset. ConvNeXt reconstructions for high-multiplexing diffuser measurements are also provided as a reference. Both the RML and the ConvNeXt reconstruction architecture contribute to image quality improvements over state-of-the-art.

low-multiplexing RML measurements, despite the improved optical encoding quality, is also worse than the ConvNeXt reconstructions for high-multiplexing diffuser measurements.

These studies demonstrate that attention-based architectures are not strictly necessary to achieve high-quality lensless image reconstruction, especially for the case of improved measurement quality with reduced multiplexing (RML). Based on our experiments, architectural capacity and training data must be matched to reconstruction architectures for best performance, as demonstrated by diminishing returns for our ConvNeXt model with dataset sizes exceeding 50,000 measurements, and sub-optimal performance for the Swin Transformer architecture despite increased model capacity.

Table 2 Reconstruction quality for models evaluated on 50,000 measurements from the Parallel Lensless Dataset.

Model	PSNR \uparrow	SSIM \uparrow
ConvNeXt Diffuser	24.20	0.714
Vision Transformer RML	23.50	0.673
Swin Transformer RML	23.20	0.674
Lensless Imaging Transformer RML	20.51	0.674
ConvRML (ours)	27.19	0.830

Our ConvNeXt reconstruction generalizes across both low and moderate data regimes, and both high- and low-multiplexing encoders, validating its suitability as a flexible reconstruction architecture for lensless imaging.

2.5 Experimental generalization to real-world objects

In previous sections, we compared optical designs and reconstruction algorithms using images displayed on a monitor under controlled illumination to facilitate large-scale data acquisition and standardized comparison. Here, we evaluate our ConvNeXt models’ generalization ability by reconstructing physical objects placed in front of the lensless imaging systems. In real-world imaging conditions, there are additional sources of variability that can present significant challenges for algorithm generalization, including object-dependent signal intensities, variations in object positions and depths, system non-idealities, and uncontrolled illumination [39].

Objects are hand-aligned for approximately equal positioning in front of each lensless imager, with inevitable variations in alignment, magnification, and FOV. While the display emits light uniformly across the object FOV, real objects require external illumination, with captured measurements relying on light reflected from object surfaces. Object specularity affects measurement quality, with matte objects requiring stronger and closer illumination than specular objects, and reflective surfaces introducing bright highlights.

Using the ConvNeXt models trained on our datasets of displayed images (Fig. 5), we reconstruct real objects for both RML and diffuser systems. Figure 1 shows reconstruction results for objects with varying materials and surface properties, including matte fabric, plastic, metal, and painted wood. Additional examples are provided in Supplement Fig. S4. Reconstructions for both systems are high quality, and the differences in resolution and image quality between the RML and diffuser system reconstructions are consistent with previous sections. The RML successfully recovers fine textures of objects with matte surfaces, including the fibers on the mushroom, the felt on the penguin, and the stitching on the dog, whereas the diffuser struggles to recover these details. Sharp edges and patterns on the plastic ducks are recovered by the RML but missed on the diffuser, and specular effects and variable illumination on the metal school bus cause distortion in the diffuser reconstruction, but not the RML.

3 Discussion

ConvRML pairs a precision-manufactured random multi-focal lenslet (RML) phase mask with a ConvNeXt convolutional neural network reconstruction architecture. Our phase mask produces high-quality measurements that preserve measurement contrast and exhibit tolerance to sensor read noise, quantization error, and axial misalignment. Our ConvNeXt reconstruction outperforms attention-based models and provides high-quality image reconstructions that generalize to real objects. Throughout this work, we standardize comparisons between lensless imaging systems with parallel data acquisition, and provide datasets of 100,000 measurements for both the RML and diffuser lensless imagers, as well as a lens system for comparison. Together, our contribution showcases image quality improvements made possible by combining advances in optical encoder design with data-driven reconstruction architectures.

The general-utility RML design used in this work supports both photography-scale lensless imaging and Fourier-plane modulation [16], prioritizing reduced multiplexing over extreme compactness while maintaining sensor-to-mask distances comparable to existing lenslet-based imagers [4]. Our RML is distinguished from previous lenslet-based systems [3, 4, 10, 11, 14–16] by the use of multi-focal lenslets for photography-scale imaging, and precise, reproducible fabrication of our optical element. Multi-focal lenslets are naturally suited for depth-varying imaging; in this design, the focal length distribution provides an extended depth of focus at photography-scale working distances. Therefore, we focus on 2D imaging with data-driven reconstruction. Future work can extend our RML design for 3D or extended FOV imaging by adjusting focal lengths and lenslet distributions, or optimize an RML design to maximize task performance and measurement quality using end-to-end [40, 41] or information-driven techniques [6, 42].

Our reconstruction approach advances pure deep learning models, which reconstruct images without explicit physics-based constraints such as a calibrated system PSF. Within this scope, our ConvNeXt architecture demonstrates better performance than attention-based architectures while maintaining moderate data and computational requirements. We found that ConvNeXt was best matched with a 50,000 measurement training dataset, but increased model capacity and other large architectures, such as the Swin Transformer, may benefit from larger training datasets. Future work can continue to explore tradeoffs between model capacity, dataset size, and practical training considerations. Incorporating calibrated system models and hybrid two-step approaches [19, 43] could further improve reconstruction quality. Finally, although the systems studied here are approximately shift-invariant, exploring ConvNeXt-based reconstruction for spatially varying systems, as well as incorporating existing spatially-varying architectures [8, 27, 44], are promising directions, especially for *in vivo* lensless imaging.

A unique contribution of our work is a parallel data acquisition system with open-source 100,000 measurement datasets for both the RML and diffuser lensless imagers. Existing open-source datasets are substantially smaller [19, 23, 39, 45, 46] and limited to high-multiplexing encoders. We provide the largest open-source lensless datasets available to date, the first open-source dataset available for lenslet-based systems, and the first dataset to support controlled evaluation of multiple systems within a single

acquisition framework, while demonstrating the high image quality possible using low-cost, off-the-shelf 8-bit sensors. Our contribution provides shared resources for continued work, supporting development of data-driven reconstruction architectures and enabling standardized evaluation of lensless imaging systems.

4 Materials and methods

Experimental setup

All imaging systems use identical low-cost board-level sensors (Basler daA1920-160uc, Sony IMX392). The sensor-to-mask distance is 16 mm for the RML and 4.5 mm for the diffuser. The lens system uses a 6 mm focal length S-mount lens (Evetar M13B0618W), which is incorporated into the optical path using a 50/50 split ratio beamsplitter (ThorLabs BS031) placed between the display and the diffuser. A system enclosure and a divider between the RML and diffuser block stray light (Supplement Fig. S6).

The RML phase mask has pseudo-random lenslet positions to minimize the PSF autocorrelation [29]. Focal lengths range from approximately 13.5 mm to 15.5 mm, supporting both 2D imaging and Fourier-plane encoding [16]. The phase mask is PDMS polymer placed in a custom-fabricated laser ablation mold (PowerPhotonic). With updated two-photon lithography techniques, the mask can also be directly fabricated [30]. A 3.02 mm by 2.65 mm aperture placed on the RML limits the PSF extent to the sensor region, with 11 lenslets in the effective aperture. The RML height profile (Supplement Fig. S5) and fabrication file [47] are also provided. The diffuser system uses a Gaussian diffuser (Luminit 0.5°) with a 4.73 by 3.33 mm aperture.

All systems are manually aligned for approximately equal magnification in the reconstructed images. System PSFs are acquired using a 532 nm (Thorlabs CPS 532) laser point source placed at the calibration plane, located 435 mm, 161 mm, and 165 mm from the RML, diffuser, and lens respectively. A portable monitor (INNOCN 13A1F) is placed at the same plane to display images. For real-world captures, objects are placed at the calibration plane and illuminated with a flashlight (iPhone 14 Pro). Camera exposure, illumination strength, and illumination distance are adjusted for each object capture.

Dataset acquisition

Our Parallel Lensless Dataset (PLD), consisting of 100,000 measurements from two lensless imagers and corresponding ground truth images from a lens system, as well as all system control, alignment, and calibration scripts, are released as open-source [47]. The PLD uses the first 100,000 images in the MIRFLICKR-1M dataset [34], which are displayed on a monitor and captured using an automatic acquisition pipeline. Images are cropped to 300×300 pixels to control for different image sizes and displayed with a black background. Two identical copies are displayed for each image, with display positions calibrated to center measurements on the corresponding sensors. Image display and capture are synchronized across systems, which allows for scalable, automatic acquisition of $100,000^+$ image datasets.

Captured images are $4\times$ downsampled to 480×300 pixels to reduce fringe effects [19] and maintain tractable memory requirements for reconstruction. Full-resolution measurements are also provided [47]. Ground truth images are corrected for lens distortion and mirrored vertically to match the orientation of the lensless imagers. Reconstructions from the RML and diffuser systems are computationally aligned to the undistorted ground truth images for quantitative comparison in the same coordinate space (Supplement Fig. S6).

System analysis

Reported MTFs are normalized and radially averaged. Mutual information (MI) estimation [33] uses an object distribution consisting of the first 10,000 natural images from the MIRFLICKR-1M [34] dataset. Each 300×300 pixel cropped image is converted to grayscale and scaled to a maximum intensity of 4096 photons, corresponding to an effective bit depth of 12 bits. Simulated measurements are generated by convolving images with experimentally measured PSFs and adding Gaussian noise with standard deviation σ in photons. For MI estimation, measurements are downsampled to 50×50 pixels and randomly sampled into 32×32 pixel patches. Information is estimated using a full Gaussian entropy model with 8000 patches used for model fitting and 2000 patches reserved for evaluation. Read noise levels from $\sigma = 1.0$ to $\sigma = 20.0$ are evaluated. Measurements with fixed read noise $\sigma = 5.0$ are quantized by adding uniform noise to simulate effective bit depths between 4 and 12 bits.

Reconstruction architectures

The ConvNeXt reconstruction architecture uses a ConvNeXt-T encoder backbone [35] followed by a Feedforward Neural Network (FNN) decoder. The encoder processes 480×300 pixel inputs through four downsampling stages with stage blocks of (3, 3, 9, 3), producing multi-scale feature representations. The decoder aggregates features using bilinear interpolation and channel-wise concatenation to the target 480×300 pixel image size, followed by five 3×3 convolutional layers with batch normalization and ReLU activations to produce a 3-channel RGB output.

The Swin Transformer [38] patches the input into 15×15 pixel patches, uses a window size of 7, a stage depth ratio of (2, 2, 6, 2), an embedding dimension of 128, and attention head counts of (4, 8, 16, 32). Multi-scale features are decoded using the same FNN decoder as ConvNeXt.

The Vision Transformer [37] consists of 6 encoder blocks with 4 attention heads and an embedding dimension of 128, using a 15×15 pixel patch size and a dropout rate of 0.1. The Vision Transformer decoder consists of four transposed 2×2 convolutional layers with stride 2, batch normalization, and ReLU activations.

The Lensless Imaging Transformer is modified to support 300×480 pixel input and output dimensions, with the remainder of the architecture unchanged from the original implementation [23]. We use a pre-trained U-Net [19] in architecture comparisons on the DLMD dataset (Fig. 4).

All models are implemented in PyTorch [48] and trained on a single NVIDIA RTX A6000 GPU, with training times reported in the Supplement Table S3 and Table S4. All models use the AdamW optimizer with a mean squared error (MSE) loss and a

batch size of 6. Input measurements are normalized to $[0, 1]$ prior to training. For evaluation, reconstruction outputs are clamped to $[0, 1]$, and PSNR and SSIM are averaged over the test set. Metrics are computed over a cropped reconstruction extent, corresponding to image sizes of 210×380 pixels and 201×201 pixels for the DLMD and PLD respectively.

DLMD dataset evaluation follows the standard data split [19], reserving the first 1000 images for testing and using the remaining 24,000 images for training. The ConvNeXt model is trained for 35 epochs using a learning rate of 5×10^{-4} and weight decay of 10^{-3} , using a linear warmup followed by cosine annealing. The Swin Transformer follows the same protocol, while the Vision Transformer is trained for 80 epochs to ensure convergence. The Lensless Imaging Transformer is trained for 240,000 steps (≈ 60 epochs) using a learning rate of 6×10^{-5} , weight decay of 10^{-1} , and the same scheduling process as ConvNeXt.

For the PLD, the first 1000 images are reserved for testing, the subsequent 4000 images for validation, and the remaining images for training. The main text uses a 50,000 measurement subset corresponding to 45,000 images for training. ConvNeXt, Swin Transformer, and Vision Transformer models follow the same training procedure as for the DLMD. The Lensless Imaging Transformer is trained for 450,000 steps (≈ 60 epochs) using a learning rate of 3×10^{-5} .

Declarations

Acknowledgments. The authors thank Fanglin Linda Liu for phase mask manufacturing and Chaoying Gu and Nick Antipa for helpful discussions.

Funding. L.A.K. was supported by the National Science Foundation Graduate Research Fellowship Program under Grant DGE 2146752. Laura Waller is a Chan Zuckerberg Biohub SF investigator. This work was supported by U.S. Air Force Office of Scientific Research Award No. FA955-22-1-0521

Conflict of interest. The authors declare no competing interests.

Code availability. All code will be released prior to publication [47].

Data availability. All data is [publicly available](#) and will be released prior to publication [47].

Author contributions. L.A.K. and L.W. conceived the idea. L.A.K., E.M., and L.W. developed the methodology. C.S.H. and L.A.K. built the experimental setup and collected the data. C.S.H. implemented the data acquisition pipeline. L.A.K. conducted the system analysis. V.P. implemented and evaluated the reconstruction architectures with assistance from L.A.K. and E.M. L.A.K. and C.S.H. produced the visualizations and figures with assistance from V.P. and L.W. L.A.K. wrote the original manuscript draft with assistance from C.S.H. All authors contributed to the review and revision of the manuscript and supplementary material. L.A.K. and L.W. supervised the project.

References

- [1] Antipa, N., Kuo, G., Heckel, R., Mildenhall, B., Bostan, E., Ng, R., Waller, L.: Diffusercam: lensless single-exposure 3d imaging. *Optica* **5**(1), 1–9 (2018) <https://doi.org/10.1364/OPTICA.5.000001>
- [2] Boominathan, V., Adams, J.K., Robinson, J.T., Veeraraghavan, A.: Phlatcam: Designed phase-mask based thin lensless camera. *IEEE Transactions on Pattern Analysis and Machine Intelligence* **42**(7), 1618–1629 (2020) <https://doi.org/10.1109/TPAMI.2020.2987489>
- [3] Xue, Y., Davison, I.G., Boas, D.A., Tian, L.: Single-shot 3d wide-field fluorescence imaging with a computational miniature mesoscope. *Science Advances* **6**(43), 7508 (2020) <https://doi.org/10.1126/sciadv.abb7508> <https://www.science.org/doi/pdf/10.1126/sciadv.abb7508>
- [4] Tian, F., Yang, W.: Learned lensless 3D camera. *Optics Express* **30**(19), 34479–34496 (2022) <https://doi.org/10.1364/OE.465933> . Publisher: Optica Publishing Group
- [5] Yao, X., Pathak, V., Xi, H., Chaware, A., Cooke, C., Kim, K., Xu, S., Li, Y., Dunn, T., Konda, P.C., Zhou, K.C., Horstmeyer, R.: Increasing a microscope’s effective field of view via overlapped imaging and machine learning. *Opt. Express* **30**(2), 1745–1761 (2022) <https://doi.org/10.1364/OE.445001>
- [6] Kabuli, L.A., Pinkard, H., Markley, E., Hung, C.S., Waller, L.: Designing lensless imaging systems to maximize information capture. *Optica* **13**(2), 227–235 (2026) <https://doi.org/10.1364/OPTICA.570334>
- [7] Hung, C.S., Kabuli, L.A., Waller, L.: Extended field-of-view lensless imaging with random multi-focal lenslet arrays. In: *Optica Imaging Congress (3D, COSI, DH, FLatOptics, IS, pcAOP)*, pp. 1–3 (2025). <https://doi.org/10.1364/COSI.2025.CTh1B.3> . Optica Publishing Group
- [8] Lee, K.C., Kim, N., Park, J., Baek, N., Bae, J., Kim, T., Bae, J., Park, W., Lee, S.A.: Extended field-of-view imaging for lensless camera using differentiable phase mask design and image deconvolution. In: *2024 Conference on Lasers and Electro-Optics Pacific Rim (CLEO-PR)* (2024). Optica Publishing Group
- [9] Tan, J., Niu, L., Adams, J.K., Boominathan, V., Robinson, J.T., Baraniuk, R.G., Veeraraghavan, A.: Face detection and verification using lensless cameras. *IEEE Transactions on Computational Imaging* **5**(2), 180–194 (2019) <https://doi.org/10.1109/TCI.2018.2889933>
- [10] Kuo, G., Liu, F.L., Grossrubatscher, I., Ng, R., Waller, L.: On-chip fluorescence microscopy with a random microlens diffuser. *Opt. Express* **28**(6), 8384–8399 (2020) <https://doi.org/10.1364/OE.382055>

- [11] Tian, F., Mattison, B., Yang, W.: DeepInMiniscope: Deep learning-powered physics-informed integrated miniscope. *Science Advances* **11**(37), 6687 (2025) <https://doi.org/10.1126/sciadv.adr6687>
- [12] Wu, J., Chen, Y., Veeraraghavan, A., Seidemann, E., Robinson, J.T.: Mesoscopic calcium imaging in a head-unrestrained male non-human primate using a lensless microscope. *Nature Communications* (15), 1271 (2024) <https://doi.org/10.1038/s41467-024-45417-6>
- [13] Asif, M.S., Ayremlou, A., Sankaranarayanan, A.C., Veeraraghavan, A., Baraniuk, R.: FlatCam: Thin, lensless cameras using coded aperture and computation. *IEEE Trans. Computational Imaging* **3**(3), 384–397 (2017) <https://doi.org/10.1109/TCI.2016.2593662>
- [14] Tian, F., Hu, J., Yang, W.: GEOMScope: Large Field-of-view 3D Lensless Microscopy with Low Computational Complexity. *Laser & Photonics Reviews* **15**(8), 2100072 (2021) <https://doi.org/10.1002/lpor.202100072>
- [15] Antipa, N., Oare, P., Bostan, E., Ng, R., Waller, L.: Video from stills: Lensless imaging with rolling shutter. In: 2019 IEEE International Conference on Computational Photography (ICCP), pp. 1–8 (2019). <https://doi.org/10.1109/ICCPHOT.2019.8747341>
- [16] Liu, F.L., Kuo, G., Antipa, N., Yanny, K., Waller, L.: Fourier diffuserscope: single-shot 3d fourier light field microscopy with a diffuser. *Opt. Express* **28**(20), 28969–28986 (2020) <https://doi.org/10.1364/OE.400876>
- [17] Boyd, S.P., Parikh, N., Chu, E., Peleato, B., Eckstein, J.: Distributed optimization and statistical learning via the alternating direction method of multipliers. *Found. Trends Mach. Learn.* **3**(1), 1–122 (2011) <https://doi.org/10.1561/2200000016>
- [18] Beck, A., Teboulle, M.: A fast iterative shrinkage-thresholding algorithm for linear inverse problems. *SIAM Journal on Imaging Sciences* **2**(1), 183–202 (2009) <https://doi.org/10.48550/arXiv.2409.17996>
- [19] Monakhova, K., Yurtsever, J., Kuo, G., Antipa, N., Yanny, K., Waller, L.: Learned reconstructions for practical mask-based lensless imaging. *Opt. Express* **27**(20), 28075–28090 (2019) <https://doi.org/10.1364/OE.27.028075>
- [20] Cai, X., You, Z., Zhang, H., Liu, W., Gu, J., Xue, T.: Phocolens: Photorealistic and consistent reconstruction in lensless imaging. *arXiv preprint arXiv:2409.17996* (2024) <https://doi.org/10.48550/arXiv.2409.17996>
- [21] Kingshott, O., Antipa, N., Bostan, E., Akşit, K.: Unrolled Primal-Dual Networks for Lensless Cameras. *Optics Express* **30**(26), 46324 (2022) <https://doi.org/10.1364/OE.475521>

- [22] Ronneberger, O., Fischer, P., Brox, T.: U-net: Convolutional networks for biomedical image segmentation. In: Navab, N., Hornegger, J., Wells, W.M., Frangi, A.F. (eds.) Medical Image Computing and Computer-Assisted Intervention – MICCAI 2015, pp. 234–241. Springer, Cham (2015). https://doi.org/10.1007/978-3-319-24574-4_28
- [23] Pan, X., Chen, X., Takeyama, S., Yamaguchi, M.: Image reconstruction with transformer for mask-based lensless imaging. *Opt. Lett.* **47**(7), 1843–1846 (2022) <https://doi.org/10.1364/OL.455378>
- [24] Khan, S., Sundar, V., Boominathan, V., Veeraraghavan, A., Mitra, K.: Flatnet: Towards photorealistic scene reconstruction from lensless measurements. *IEEE Transactions on Pattern Analysis & Machine Intelligence* (2020) <https://doi.org/10.1109/TPAMI.2020.3033882>
- [25] Kabuli, L.A., Singh, N.M., Waller, L.: Estimation-theoretic analysis of lensless imaging. In: Computational Optical Imaging and Artificial Intelligence in Biomedical Sciences II, vol. 13333, p. 1333307 (2025). <https://doi.org/10.1117/12.3043676> . SPIE
- [26] Liu, Z., Zeng, T., Zhan, X., Zhang, X., Lam, E.Y.: Generative approach for lensless imaging in low-light conditions. *Optics Express* **33**(2), 3021 (2025) <https://doi.org/10.1364/oe.544875>
- [27] Yang, Q., Guo, R., Hu, G., Xue, Y., Li, Y., Tian, L.: Wide-field, high-resolution reconstruction in computational multi-aperture miniscope using a fourier neural network. *Optica* **11**(6), 860–871 (2024) <https://doi.org/10.1364/OPTICA.523636>
- [28] Yanny, K., Monakhova, K., Shuai, R.W., Waller, L.: Deep learning for fast spatially varying deconvolution. *Optica* **9**(1), 96–99 (2022) <https://doi.org/10.1364/OPTICA.442438>
- [29] Kabuli, L., Gu, C., Waller, L.: Replica artifacts in phase mask-based lensless imaging systems. In: Optica Imaging Congress (3D, COSI, DH, FFlatOptics, IS, pcAOP). COSI (2023). <https://doi.org/10.1364/cosi.2023.cw3b.4> . Optica Publishing Group. pages CW3B.4
- [30] Sartison, M., Weber, K., Thiele, S., Bremer, L., Fischbach, S., Herzog, T., Kolatschek, S., Jetter, M., Reitzenstein, S., Herkommer, A., Michler, P., Portalupi, S.L., Giessen, H.: 3d printed micro-optics for quantum technology: Optimised coupling of single quantum dot emission into a single-mode fibre. *Light: Advanced Manufacturing* **2**, 103 (2021) <https://doi.org/10.37188/lam.2021.006>
- [31] Kabuli, L., Wu, G., Waller, L.: High-quality lensless imaging with a random multi-focal lenslet phase mask. In: Optica Imaging Congress (3D, COSI, DH, FFlatOptics, IS, pcAOP) (2023). <https://doi.org/10.1364/COSI.2023.CW3B.2> . Optica Publishing Group. pages CW3B.2

[32] Li, S., Gao, Y., Wu, J., Wang, M., Huang, Z., Chen, S., Cao, L.: Lensless camera: Unraveling the breakthroughs and prospects. *Fundamental Research* **5**(4), 1725–1736 (2025) <https://doi.org/10.1016/j.fmre.2024.03.019>

[33] Pinkard, H., Kabuli, L., Markley, E., Chien, T., Jiao, J., Waller, L.: Information-driven design of imaging systems. In: *The Thirty-ninth Annual Conference on Neural Information Processing Systems* (2025). arXiv:2405.20559. <https://openreview.net/forum?id=R9MUFuXG2o>

[34] Mark J. Huiskes, B.T., Lew, M.S.: New trends and ideas in visual concept detection: The MIR Flickr retrieval evaluation initiative. In: *Proceedings of the 2010 ACM International Conference on Multimedia Information Retrieval*, pp. 527–536. ACM, New York, NY, USA (2010). <https://doi.org/10.1145/1743384.1743475>

[35] Todi, A., Narula, N., Sharma, M., Gupta, U.: Convnext: A contemporary architecture for convolutional neural networks for image classification. In: *2023 3rd International Conference on Innovative Sustainable Computational Technologies (CISCT)*, pp. 1–6 (2023). <https://doi.org/10.1109/CISCT57197.2023.10351320>

[36] Ding, X., Zhang, X., Han, J., Ding, G.: Scaling up your kernels to 31×31 : Revisiting large kernel design in cnns. In: *2022 IEEE/CVF Conference on Computer Vision and Pattern Recognition (CVPR)*, pp. 11953–11965 (2022). <https://doi.org/10.1109/CVPR52688.2022.01166>

[37] Dosovitskiy, A., Beyer, L., Kolesnikov, A., Weissenborn, D., Zhai, X., Unterthiner, T., Dehghani, M., Minderer, M., Heigold, G., Gelly, S., Uszkoreit, J., Houlsby, N.: An Image is Worth 16x16 Words: Transformers for Image Recognition at Scale. arXiv (2020). <https://doi.org/10.48550/ARXIV.2010.11929> . <https://arxiv.org/abs/2010.11929>

[38] Liu, Z., Lin, Y., Cao, Y., Hu, H., Wei, Y., Zhang, Z., Lin, S., Guo, B.: Swin transformer: Hierarchical vision transformer using shifted windows. In: *Proceedings of the IEEE/CVF International Conference on Computer Vision (ICCV)* (2021). <https://doi.org/10.1109/ICCV48922.2021.00986>

[39] Bezzam, E., Peters, S., Vetterli, M.: Let there be light: Robust lensless imaging under external illumination with deep learning. In: *ICASSP 2025 - 2025 IEEE International Conference on Acoustics, Speech and Signal Processing (ICASSP)*, pp. 1–5 (2025). <https://doi.org/10.1109/ICASSP49660.2025.10888030>

[40] Shi, W., Huang, Z., Huang, H., Hu, C., Chen, M., Yang, S., Chen, H.: LOEN: Lensless opto-electronic neural network empowered machine vision. *Light Sci. Appl.* **11**(1), 121 (2022) <https://doi.org/10.1038/s41377-022-00809-5>

[41] Sitzmann, V., Diamond, S., Peng, Y., Dun, X., Boyd, S., Heidrich, W., Heide, F., Wetzstein, G.: End-to-end optimization of optics and image processing for

achromatic extended depth of field and super-resolution imaging. *ACM Trans. Graph.* **37**(4) (2018) <https://doi.org/10.1145/3197517.3201333>

[42] Markley, E., Pinkard, H., Kabuli, L., Singh, N., Waller, L.: Computationally efficient information-driven optical design with interchanging optimization. arXiv (2025) <https://doi.org/10.48550/arXiv.2507.07789> . arXiv:2507.07789

[43] Poudel, A., Nakarmi, U.: Deeplir: Attention-based approach for mask-based lensless image reconstruction. In: 2024 IEEE/CVF Winter Conference on Applications of Computer Vision Workshops (WACVW), pp. 431–439 (2024). <https://doi.org/10.1109/WACVW60836.2024.00052>

[44] Xue, Y., Yang, Q., Hu, G., Guo, K., Tian, L.: Deep-learning-augmented computational miniature mesoscope. *Optica* **9**(9), 1009–1021 (2022) <https://doi.org/10.1364/OPTICA.464700>

[45] Bezzam, E., Perron, Y., Vetterli, M.: Towards robust and generalizable lensless imaging with modular learned reconstruction. *IEEE Transactions on Computational Imaging* **11**, 213–227 (2025) <https://doi.org/10.1109/TCI.2025.3539448>

[46] Hung, C.S., Kabuli, L.A., Ponomarenko, V., Waller, L.: Scalable dataset acquisition for data-driven lensless imaging. In: Computational Optical Imaging and Artificial Intelligence in Biomedical Sciences II, vol. 13333, pp. 54–58 (2025). <https://doi.org/10.1117/12.3040992> . SPIE

[47] Kabuli, L.A., Hung, C.S., Ponomarenko, V., Markley, E., Waller, L.: Code for “ConvRML: High-Quality Lensless Imaging with Random Multi-Focal Lenslets”. <https://github.com/lakabuli/ConvRML>

[48] Paszke, A., Gross, S., Massa, F., Lerer, A., Bradbury, J., Chanan, G., Killeen, T., Lin, Z., Gimelshein, N., Antiga, L., Desmaison, A., Kopf, A., Yang, E., DeVito, Z., Raison, M., Tejani, A., Chilamkurthy, S., Steiner, B., Fang, L., Bai, J., Chintala, S.: PyTorch: An Imperative Style, High-Performance Deep Learning Library. arXiv (2019). <https://doi.org/10.48550/ARXIV.1912.01703> . <https://arxiv.org/abs/1912.01703>

[49] Lee, K.C., Bae, J., Baek, N., Jung, J., Park, W., Lee, S.A.: Design and single-shot fabrication of lensless cameras with arbitrary point spread functions. *Optica* **10**(1), 72–80 (2023) <https://doi.org/10.1364/OPTICA.466072>

[50] Yanny, K., Antipa, N., Liberti, W., Dehaeck, S., Monakhova, K., Liu, F.L., Shen, K., Ng, R., Waller, L.: Miniscope3D: optimized single-shot miniature 3D fluorescence microscopy. *Light: Science & Applications* **9**(1), 171 (2020) <https://doi.org/10.1038/s41377-020-00403-7>

[51] Pygame Community: Pygame: Python Game Development Library. <https://www.pygame.org/>. Version 2.6.1 (2024)

- [52] Bradski, G.: The OpenCV Library. Dr. Dobb's Journal of Software Tools (2000)
- [53] Riba, E., Mishkin, D., Ponsa, D., Rublee, E., Bradski, G.: Kornia: an open source differentiable computer vision library for pytorch. In: Winter Conference on Applications of Computer Vision (2020). <https://arxiv.org/pdf/1910.02190.pdf>

Supplementary material for ConvRML: High-Quality Lensless Imaging with Random Multi-Focal Lenslets

This supplementary material contains additional results and implementation details.

S1 Additional reconstruction architecture evaluations

Training dataset size

We investigate how training dataset size affects reconstruction performance using our 100,000 measurement Parallel Lensless Dataset (PLD). We study the tradeoffs between model capacity, dataset size, and training cost by training the ConvNeXt architecture on subsets of 25,000, 50,000, 75,000, and all 100,000 of the RML measurements from the PLD.

Figure S1 reports reconstruction performance as a function of training dataset size. Reconstruction quality improves as the dataset size increases from 25,000 to 50,000 measurements. After 50,000 measurements, reconstruction quality plateaus while training time increases significantly (Table S1), indicating that the capacity of the ConvNeXt model is best matched to 50,000 measurements. Therefore, we use 50,000 measurements as our standard training dataset size for all relevant evaluations and comparisons.

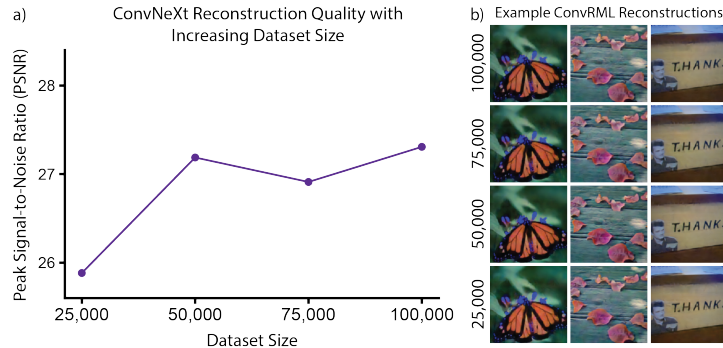


Fig. S1 Effect of training dataset size on ConvNeXt reconstruction quality for random multi-focal lenslet (RML) measurements from the Parallel Lensless Dataset. Reconstruction quality improves as dataset size increases from 25,000 to 50,000 measurements and plateaus after 50,000 measurements, indicating that model capacity is best matched to 50,000 measurements.

Table S1 ConvNeXt training times with increasing dataset size for random multi-focal lenslet (RML) measurements.

Dataset size	Training time (hrs)
25,000	86
50,000	210
75,000	336
100,000	476

Inference and training times

We report inference times for a single image reconstruction in Table S2. The inference time for ConvNeXt is shorter than both the large Swin Transformer and the Lensless Imaging Transformer [23]. Inference times were calculated by averaging 100 reconstruction passes on an NVIDIA RTX A6000 GPU after 10 warmup iterations, with GPU synchronization. As the Lensless Imaging Transformer reconstructs one channel at a time, its inference time for one RGB image corresponds to three sequential channel reconstructions.

Table S2 Single image reconstruction inference time for each model evaluated on the DiffuserCam Lensless Mirflickr Dataset (DLMD) and Parallel Lensless Dataset (PLD).

Model	DLMD inference (ms)	PLD inference (ms)
U-Net	3.77	N/A
Vision Transformer	3.18	3.16
Swin Transformer	63.3	68.3
Lensless Imaging Transformer	128	137
ConvNeXt	48.3	52.3

We report model training times and memory usage for the Parallel Lensless Dataset (PLD) in Table S3 and for the DiffuserCam Lensless Mirflickr Dataset (DLMD) in Table S4, using the same number of training epochs for both datasets. ConvNeXt has training times comparable to the Lensless Imaging Transformer for both datasets, while maintaining less memory usage than the Swin Transformer throughout.

Table S3 Training times and memory usage for all models trained on 50,000 RML measurements from the Parallel Lensless Dataset (PLD).

Model	Epochs	Training time (hrs)	GPU memory
Vision Transformer	80	293	1 GB
Swin Transformer	35	445	30 GB
Lensless Imaging Transformer	60	211	21 GB
ConvNeXt	35	210	32 GB

Table S4 Training times and memory usage for all models trained on the DiffuserCam Lensless Mirflickr Dataset (DLMD).

Model	Training time (hrs)	GPU memory
Vision Transformer	54	1 GB
Swin Transformer	279	33 GB
Lensless Imaging Transformer	90	19 GB
ConvNeXt	100	29 GB

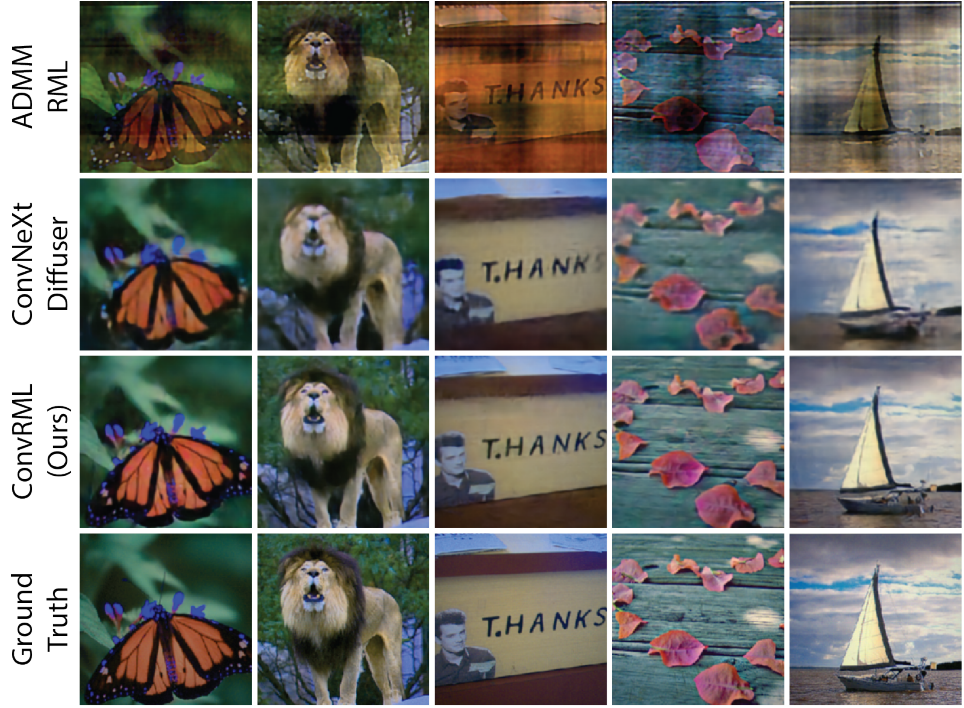


Fig. S2 Comparison of ConvNeXt and iterative alternating direction method of multipliers (ADMM) reconstruction. ADMM reconstructions of random multi-focal lenslet (RML) measurements have visible image artifacts and reduced image quality, while the ConvNeXt reconstructions for both RML and diffuser measurements closely match the ground truth images.

Reconstruction quality with iterative reconstruction

In Fig. S2, we compare reconstruction quality with our ConvNeXt model for diffuser and RML measurements to iterative reconstruction using 5 iterations of alternating direction method of multipliers (ADMM) [17] for RML measurements. ADMM reconstruction uses parameters $\mu_1 = 1e^{-6}$, $\mu_2 = 1e^{-4}$, $\mu_3 = 4e^{-5}$, $\tau = 2e^{-3}$ and reconstructs a single image in 225 ms. ConvNeXt's pure deep learning-based approach provides significant quality improvement over ADMM's artifact-prone reconstructions, without any knowledge of the RML system point spread function (PSF) or image formation model.

S2 Modulation transfer function evaluation

In addition to the parallel system evaluation in the main text, we evaluate the frequency transfer abilities of our RML compared to the PhlatCam phase mask [2], a heuristically-designed mask with a high-multiplexing caustic pattern. In Fig. S3, we compute the modulation transfer function (MTF) for each system's point spread function (PSF). Since the PhlatCam phase mask is not included in our parallel system

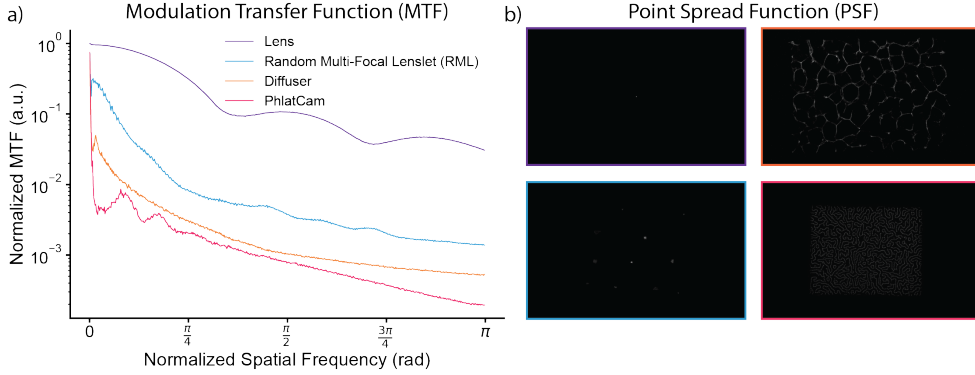


Fig. S3 Modulation transfer function (MTF) evaluation. a) MTFs for random multi-focal lenslet (RML), diffuser, and PhlatCam point spread functions (PSF) using the lens as an ideal reference. The RML has improved frequency transfer compared to both the diffuser and PhlatCam. b) PSFs for each imaging system.

setup, we use a publicly available PSF capture [2], which is cropped to match the aspect ratio of our sensors and rescaled to the same spatial dimensions prior to MTF computation. The RML has superior frequency transfer compared to both PhlatCam and the diffuser. Notably, the diffuser PSF also outperforms the PhlatCam PSF, in contrast with prior MTF evaluations [2, 4]. This finding highlights both the sensitivity of MTF analysis to experimental conditions and the variability inherent to Gaussian diffusers. These comparisons emphasize the importance of standardized evaluation and reproducible optical fabrication when comparing lensless imaging phase masks.

S3 Real object reconstructions

We provide additional reconstructions of real objects with varying materials and surface properties in Fig. S4. ConvRML recovers fine details and textures, whereas ConvNeXt reconstructions of diffuser measurements are blurred, as illustrated by the inset of the fibers on the felt mushroom. ConvRML also recovers the patterns on the duck torso while tolerating non-uniform illumination and specular effects, which introduce distortions in diffuser reconstructions. Minor differences in position and magnification are due to the practical limitations of manual object alignment across imaging systems.

S4 Random multi-focal lenslet phase mask

Figure S5 visualizes the height map used to generate the RML phase mask, with a white rectangle indicating the active aperture region (3.02 mm by 2.65 mm) used for the RML system. For fabrication, the height map is defined on a 750×750 pixel surface grid, with 10 μm pixel pitch, corresponding to a total fabrication area of 7.5×7.5 mm. The design file is provided with the PLD [47].



Fig. S4 Additional real object reconstructions. Reconstructions of real objects with varying surface properties using ConvNeXt architectures trained on displayed image datasets for the RML (top) and diffuser (bottom) lensless imaging systems.

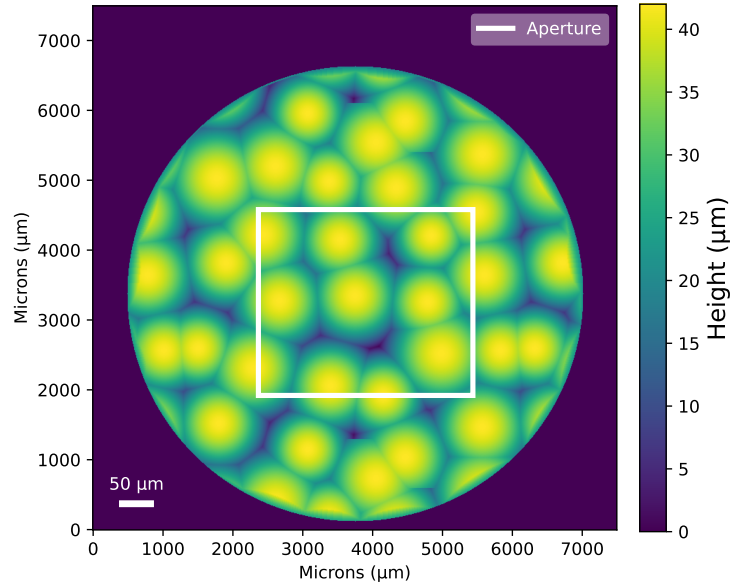


Fig. S5 Height map for generating the random multi-focal lenslet (RML) phase mask. Surface height map for the RML design defined on grid with $10\text{ }\mu\text{m}$ pixel pitch. The white rectangle indicates the active region including the aperture placed on the fabricated optical element.

Lenslet-based designs have been constrained by the lack of fabrication techniques capable of producing freeform optical elements with controlled surface variations. Two-photon lithography used for caustic phase mask fabrication [2, 49] faced limitations in modulation depth, surface discretization, and large FOV stitching [50], which restricted its utility for realizing smooth multi-focal lenslet designs. As a result, systems have relied on alternative, often manual, approaches that constrain the mask design space or limit precise surface control, limiting reproducibility and overall system quality. For example, microscopy-scale designs utilized multi-focal phase

masks produced using mechanically-dented molds [16], droplet curing [10], or hand-arranged uni-focal lenslets [11]. Macro-scale designs consist of off-the-shelf regular lenslet arrays [3, 27, 44] as well as random uni-focal arrays made with mechanically-dented [15] or 3D printed molds [4, 14]. Our RML is distinguished from previous lenslet-based systems by the use of multi-ofcal lenslets for photography-scale imaging and precise, reproducible fabrication of our optical element. Large-area grayscale lithography [30] and freeform optical element manufacturing have resolved many of the fabrication constraints faced by earlier systems, providing the necessary capabilities to manufacture our multi-focal design.

S5 Parallel Lensless Dataset implementation

For parallel system capture, the RML and diffuser systems are aligned to a display, with the lensed camera incorporated into the optical path of the diffuser with a beam-splitter (Fig. S6a). We control for stray light using an enclosure placed around the parallel imaging system and non-reflective dividers between the RML and diffuser. Each sensor is mounted to standard 2-inch optical components with custom 3D-printed adapters. A step-by-step tutorial and computer-aided design files are provided with the PLD [47].

Automated dataset acquisition

The Parallel Lensless Dataset (PLD) consists of the first 100,000 images of the MIRFLICKR-1M dataset [34]. We automatically display images with a Python acquisition script that uses the Pygame package [51].

Image display and data capture are synchronized across the three cameras with a 200 ms delay between each camera and a 500 ms delay between each image to ensure reliable image buffer saving. Sensor exposure times are calibrated using a reference measurement and set to 80 ms for RML, 50 ms for diffuser, and 4 ms for lens. Captured measurements are saved directly to an external solid-state drive (SanDisk SDSSDE61-2T00-G25). All system control scripts are released along with the PLD [47].

Ground truth image registration

Reconstructions from the RML and diffuser systems are computationally registered to ground truth images (Fig. S6b) for quantitative evaluation. To correct for lens distortion in ground truth measurements, we calibrate the distortion profile using the OpenCV 11 \times 4 asymmetric circle grid [52]. Ground truth measurements are mirrored across the y -axis to address the inversion introduced by the lens.

For pixel-level alignment between lensless reconstructions and ground truth images, we estimate a transformation matrix (homography) from each lensless imager to the ground truth images using Kornia [53]. This transformation corrects for shifts, rotations, and scale differences that cannot be fully corrected with manual optical alignment. Each homography is heuristically initialized and calibrated with 4 \times down-sampled images reconstructed with 200 iterations of FISTA [18]. For the diffuser, the homography is manually adjusted due to poor image quality in FISTA reconstructions. The color artifacts along the border of diffuser and RML reconstructions in Fig. S6b

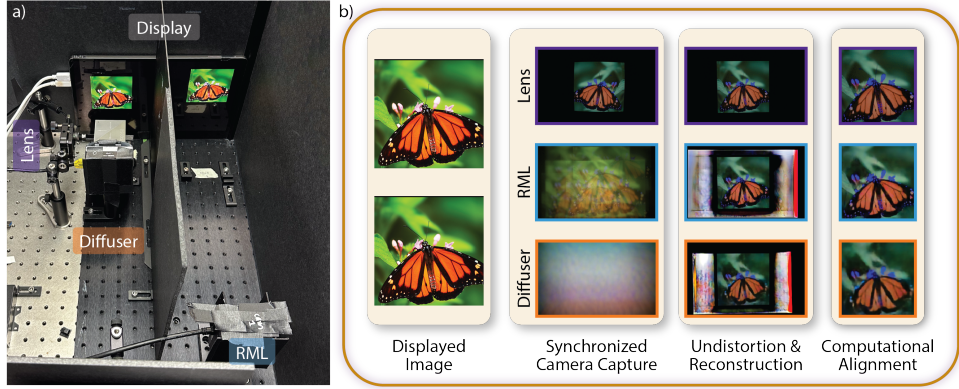


Fig. S6 Parallel dataset acquisition system and processing pipeline. a) Experimental hardware setup with the RML and diffuser in parallel and a lens system incorporated with a beamsplitter. b) Images from the MIRFLICKR-1M [34] dataset are displayed and captured synchronously by all three systems. Lens distortion and mirroring are corrected for the ground truth measurements from the lensed system, and RML and diffuser reconstructions are registered to the ground truth image and cropped to the center of the field-of-view.

are introduced by the ConvNeXt-based reconstruction, which is trained on a cropped field-of-view. Regions outside this crop are not constrained during training.